ACS APPLIED MATERIALS & INTERFACES

www.acsami.org Research Article

Extracellular Matrix/Amorphous Magnesium Phosphate Bioink for 3D Bioprinting of Craniomaxillofacial Bone Tissue

Nileshkumar Dubey, Jessica A. Ferreira, Jos Malda, Sarit B. Bhaduri, and Marco C. Bottino*

Cite This: *ACS Appl. Mater. Interfaces* 2020, 12, 23752−23763 Read Online

ABSTRACT: Bioprinting, a promising field in regenerative medicine, holds great potential to create three-dimensional, defect-specific vascularized bones with tremendous opportunities to address unmet craniomaxillofacial reconstructive challenges. A cytocompatible bioink is a critical prerequisite to successfully regenerate functional bone tissue. Synthetic self-assembling peptides have a nanofibrous structure resembling the native extracellular matrix (ECM), making them an excellent bioink component. Amorphous magnesium phosphates (AMPs) have shown greater levels of resorption while maintaining high biocompatibility, osteoinductivity, and low inflammatory response, as compared to their calcium phosphate counterparts. Here, we have established a novel bioink formulation (ECM/AMP) that combines an ECM-based hydrogel containing 2% octapeptide FEFEFKFK and 98% water with AMP particles to realize high cell function with desirable bioprintability. We analyzed the osteogenic differentiation of dental pulp stem cells (DPSCs) encapsulated in the bioink, as well as *in vivo* bone regeneration, to define the potential of the formulated bioink as a growth factor-free bone-forming strategy. Cell-laden AMP-modified bioprinted constructs showed an improved cell morphology but similar cell viability (∼90%) compared to their AMP-free counterpart. In functional assays, the cell-laden bioprinted constructs modified with AMP exhibited a high level of mineralization and osteogenic gene expression without the use of growth factors, thus suggesting that the presence of AMP-triggered DPSCs' osteogenic differentiation. Cell-free ECM-based bioprinted constructs were implanted *in vivo*. In comparison with the ECM group, bone volume per total volume for ECM/1.0AMP was approximately 1.7- and 1.4-fold higher at 4 and 8 weeks, respectively. Further, a significant increase in the bone density was observed in ECM/1.0AMP from 4 to 8 weeks. These results demonstrate that the presence of AMP in the bioink significantly increased bone formation, thus showing promise for *in situ* bioprinting strategies. We foresee significant potential in translating this innovative bioink toward the regeneration of patient-specific bone tissue for regenerative dentistry.

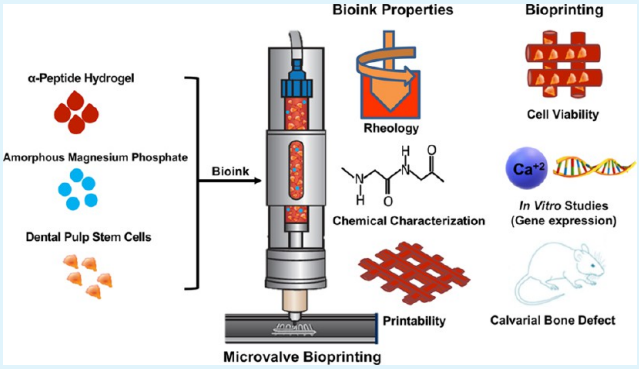

KEYWORDS: *bioprinting, amorphous magnesium phosphate, bone, regeneration, bioink*

INTRODUCTION

Bone is a dynamic organ providing a structural support and protection to the body; it undergoes remodeling to maintain its health and promote the repair of injuries.[1] Clinically speaking, craniomaxillofacial bone injuries are induced by infection, traumatic tooth extractions, periodontal disease, and oral cancer.[1] Depending on the injury type, extension, and depth, the innate healing ability of the bone may be dramatically reduced and/or inhibited.[2] Established therapeutics based on the use of natural grafts have been employed to promote repair and regeneration of the functional bone; however, 30% provide unsatisfactory clinical results.[3] Hence, various degradable or nondegradable scaffolds fabricated out of metals, polymers, hydrogels, and ceramics have been developed, aiming to provide an appropriate microenvironment for bone regeneration.[4,5] However, with the conventional tissue engineering approach, it is difficult to generate scaffolds of a specific dimension and size to cover large craniomaxillofacial defects of complex anatomy.[6]

Bioprinting, a promising field in regenerative medicine, holds great potential for creating a three-dimensional (3D) defect-specific vascularized bone from a variety of biomaterials and cells.[7,8] Two main types of bioprinting approaches have been explored to address challenges in regenerative medicine: namely, drop-on-demand (DOD) (*e.g.*, inkjet and microvalve-

Received: March 23, 2020
Accepted: April 30, 2020
Published: April 30, 2020

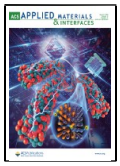

https://dx.doi.org/10.1021/acsami.0c05311
ACS Appl. Mater. Interfaces 2020, 12, 23752−23763

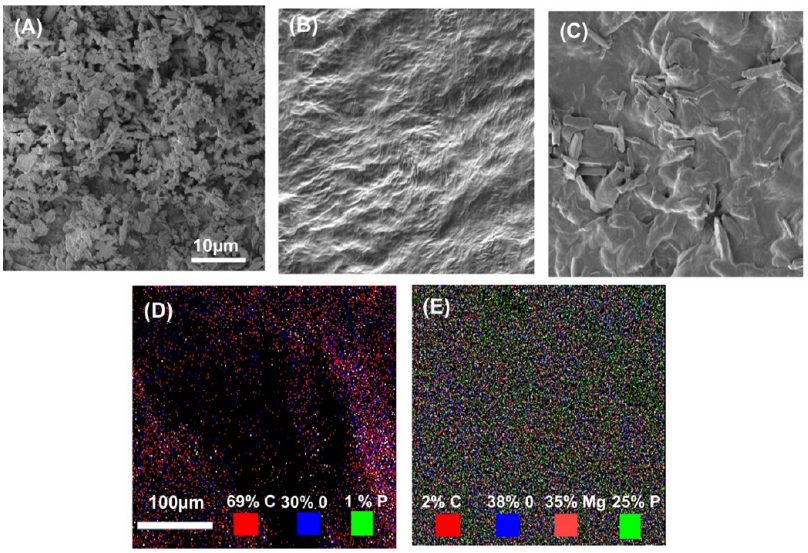

Figure 1. (A−C) SEM micrographs of AMP powder, ECM bioink, and AMP-modified bioink. (D,E) SEM−EDS mapping showing the presence of magnesium and phosphorous in the AMP-modified bioink (green: phosphorous, light red: magnesium).

based) and extrusion-based continuous printing.[9−11] Extrusion is the most commonly used method; however, creating constructs with accurate cellular positioning is challenging.[12] The DOD system offers control over the deposition of the material volume to fabricate spatially complex 3D cell-laden constructs.[9,13] Of note, the microvalve-based system offers constructs with good cell viability (>95%).[14,15] Nonetheless, regeneration of functional and vascularized bone tissue will depend on key factors, such as structural fidelity, cell proliferation, differentiation, and construct degradation.[16,17]

Natural and synthetic hydrogels possess excellent biological properties and modulus tunability to facilitate the osteogenic differentiation of mesenchymal stem cells.[16] Another advantage of hydrogels relates to the hydrophilic polymeric 3D networks that can host cells and therapeutic agents to stimulate the host response.[18,19] There are several advantages in using synthetic, self-assembling peptide hydrogels, including the fact that amino acids can easily be metabolized by enzymes *in vivo*.[20] Synthetic peptide hydrogels are repeated units of α-helixes or β-sheets of amino acids that subsequently stack to form a nanofiber that resembles the native extracellular matrix (ECM).[21] A diverse range of properties is made available through changing both the amino acids present and their order within the peptide sequence to regulate cell growth, fate, and behavior. The peptide-based hydrogel can be loaded with bioceramics, and these composites have excellent bone regenerative potential.[22] Over the years, calcium phosphate (CaP) bioceramics have been exploited because of their similarity to the mineral component of native bone tissue. More recently, cell-laden hydrogels modified with CaP have been used to print bone tissue constructs with a high degree of reproducibility.[21,22] However, CaP bioceramics generally display an acidic setting reaction and resorb too slowly, thus necessitating extremely long periods for being completely replaced by the native bone.[23,24]

Magnesium phosphates (MgPs) are considered a great alternative to CaP and have been extensively used in orthopedics for bone regeneration.[23,25−28] Studies have shown that local magnesium release could enhance the activities of osteoclasts and osteoblasts.[27] Importantly, amorphous magnesium phosphate (AMP) has been found to promote rapid differentiation and mineralization of pre-osteoblasts compared to its crystalline counterpart due to high solubility.[26,29] We have previously demonstrated that the presence of AMP in a biopolymer scaffold enhances the osteogenic gene expression of pre-osteoblasts and forms bone-like apatite when incubated in simulated body fluid.[30,31] Regardless of the promising osteogenic potential, AMP has not been used as a component of bioinks for 3D bioprinting. The hypothesis tested here is that AMP incorporation into an ECM hydrogel can trigger the osteogenic differentiation of encapsulated dental pulp stem cells (DPSCs) without any additional use of growth factors and stimulate bone regeneration *in vivo*.

Here, we report the development of a tissue-specific bioink consisting of an ECM hydrogel and AMP that enables plotting of 3D constructs with high shape fidelity and osteogenic potential. We refer to this novel composite bioink as ECM/AMP. Distinct AMP-modified bioinks (ECM/0.5AMP and ECM/1.0AMP) with suitable rheological properties were evaluated for printability and the ability to provide an appropriate microenvironment for cell encapsulation. *In vitro* cellular responses, including mineralization potential and osteogenic gene expression, were evaluated by encapsulating DPSCs, and they were cultured without osteogenic media. Furthermore, the clinical potential of our bioink for *in situ* printing was evaluated by implantation of cell-free ECM/AMP bioprinted constructs in the rat calvarial defect model. Thus, the aims of this study were to determine the effects of novel ECM/AMP bioink to control DPSCs' osteogenic commitment, and to provide a proof-of-concept validation for *in situ* use in craniomaxillofacial bone tissue engineering.

■ RESULTS AND DISCUSSION

Characterization of the ECM/AMP Bioink and Printability. The surface morphology of the AMP particles, ECM, and developed bioink was studied by scanning electron microscopy (SEM). Figure 1A demonstrates AMP powder comprises micron-sized particles with plate-like structures. Meanwhile, the SEM micrograph of the ECM reveals the presence of a tight, dense, and wrinkled surface (Figure 1B)

https://dx.doi.org/10.1021/acsami.0c05311
ACS Appl. Mater. Interfaces 2020, 12, 23752−23763

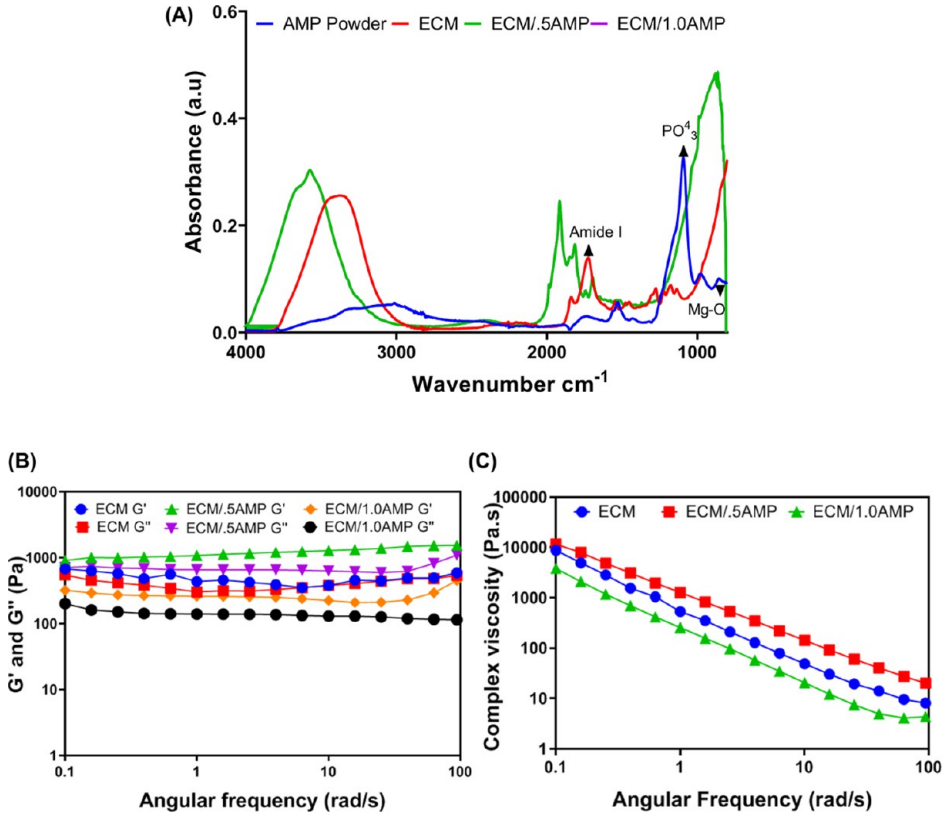

Figure 2. (A) FTIR spectra of the formulated ECM/AMP bioinks. (B,C) Rheological characterization of the bioinks showing storage modulus (G'), loss modulus (G''), and complex viscosity.

that appeared rougher because of the presence of AMP (Figure 1C). The presence of AMP in the ECM can increase the surface area and facilitate cell attachment by providing an anchorage point to the cells.[32,33] To corroborate the presence of AMP in ECM/AMP bioink, energy-dispersive X-ray spectroscopy (EDS) was performed. Figure 1D,E shows the elemental mapping of the bioink. The green and light red marked points represent the site of "P" and "Mg" in the AMP. As expected, Mg (light red) was not observed in the ECM (Figure 1D). These findings indicate that AMP was appropriately incorporated and dispersed into the bioink.

Chemical characterization of the formulated ECM/AMP bioinks was done by Fourier transform infrared (FTIR) to confirm formation of the network and investigate the presence of signature peaks of the ECM and AMP. Figure 2A shows the amide I peak at 1643 cm^{-1}, indicating the backbone of the ECM hydrogel characteristic of an α-helical conformation of self-assembly peptides.[21] AMP-related peaks at 862 and 900−1200 cm^{-1} are due to stretching vibrations of Mg^{2+} and PO_4^{3-}.[30,34] The FTIR spectra of the ECM/AMP show the characteristic peak of amide I, along with a broad phosphate peak from 500 to 1200 cm^{-1}, which can be due to alteration of the surface chemical environment causing different isotropic chemical shifts for phosphate.

The bioprinting of the cell-laden hydrogel is a disruptive technique that promotes healing of large bone defects with limited regenerative capacity.[33,35] It combines physical and biological properties to attain a 3D composite structure with homogenous cell distribution, proliferation, and differentiation overcoming the disadvantages associated with cell-free scaffold strategies.[10] Moreover, peptide hydrogels are inherently biocompatible and degradable. As a consequence, they have been used in a variety of applications, including but not limited to tissue engineering and drug delivery.[36,37] Noteworthy, water entrapment during the self-assembly process can prevent cellular dehydration, making it an ideal ink for the printing of cells. They can be further modified to provide additional biological or chemical cues, which could aid in the development of tissue-specific bioinks.[36] It is well-documented that the printability of cell-laden hydrogels is correlated with the material's rheological behavior. As such, the rheological properties of a bioink require careful consideration.[11] A pseudoplastic or shear-thinning behavior improves printability, while safeguarding the cells against excessive shear forces.[38] Figure 2B,C show the complex viscosity, where the ECM hydrogel demonstrates shear-thinning behavior, that is, the viscosity decreases as the shear rate increases. Research has shown that the addition of monodisperse inorganic particles promotes a shear-thinning behavior on the hydrogel due to particle interaction.[39] Hence, we examined the viscosity of both the ECM with AMP at different mixing ratios as a function of the shear rate. The addition of the ECM/0.5AMP increased the complex viscosity, whereas the ECM/1.0AMP decreased the viscosity. However, there was no detrimental effect on the shear-thinning properties of the formulated bioink, as the apparent shear-thinning ability was not significantly disrupted. Moreover, the storage modulus (G') and loss modulus (G'') values primarily remained higher in all groups, thus indicating a viscoelastic gel behavior with 0.5% AMP showing the highest value. At 1 rad/s, the G' for the ECM/0.5AMP is 1083 Pa compared to 435 and 260 Pa for only the ECM and ECM/1.0AMP, respectively. The ECM/1.0AMP possesses a G' value close to the ECM hydrogel,

https://dx.doi.org/10.1021/acsami.0c05311
ACS Appl. Mater. Interfaces 2020, 12, 23752−23763

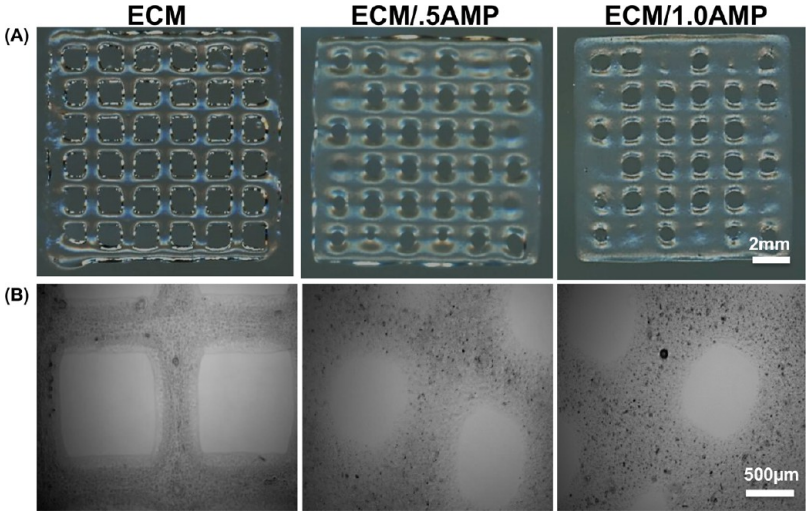

Figure 3. (A) 3D printed grid-like structures with sharp turns demonstrate the porous nature of the finalized construct. (B) Optical microscope image showing distribution of AMP particles in the printed constructs (black dot: AMP particles).

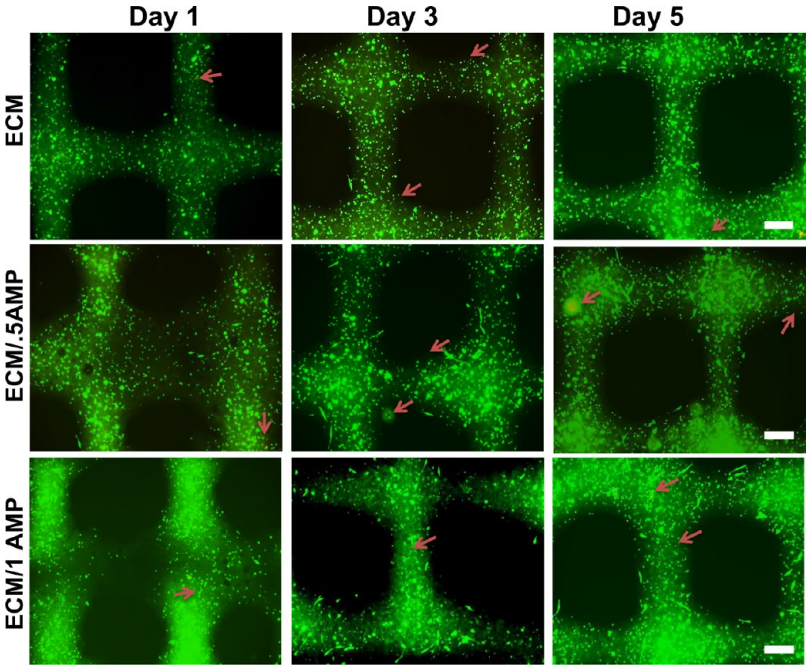

Figure 4. Calcein AM (green) and PI (red) staining assay for live and dead analysis of DPSCs after 1, 3, and 5 days in the cell-laden ECM and ECM/AMP-bioprinted constructs (red arrows: dead cells). DPSCs show an elongated morphology in AMP-modified constructs.

indicating that a similar elastic effect may occur during printing.[40]

To observe printability of the as-received ECM bioink and AMP-modified formulations, we then investigated the effect of the AMP concentration on shape fidelity. The bioink ECM/1.0AMP composition required a higher feed-rate and lower extrusion pressure for desirable print outcomes when compared to the ECM/0.5AMP. This was due to different profiles of loss modulus and storage modulus of the analyzed bioinks of the ECM/1.0AMP composition, showing the lowest storage modulus requiring less pressure to eject the fluid volume. Upon gross examination, the ECM/AMP constructs maintained a similar structural integrity compared to the pristine ECM bioink. Figure 3A shows 3D-printed grid-like structures with sharp turns and regular lines; however, with an increase in the AMP concentration, the line width increased, which may be due to the long recovery time of the formulated bioink.[28] Sedimentation of inorganic particles in the cartridge can affect printability and cell viability by blocking the printing valve and generating shear forces.[40,41] Therefore, we investigated the ability of an automated cell-mixing system to promote homogenous distribution of the AMP particles. Direct observation of AMP-modified constructs under an optical microscope showed particles with uniform sizes evenly distributed within the 3D-printed constructs (Figure 3B).

***In Vitro* Cell Viability of DPSC-Laden 3D-Printed Constructs.** The development of functional tissues from cell-laden hydrogels after bioprinting depends on the ability of the printed constructs to maintain cellular homeostasis. During the printing process, dispensing pressure and shear stress generated by the system and postprinting culture can influence cell viability.[38,40] Therefore, a cell viability assay was conducted

https://dx.doi.org/10.1021/acsami.0c05311
ACS Appl. Mater. Interfaces 2020, 12, 23752−23763

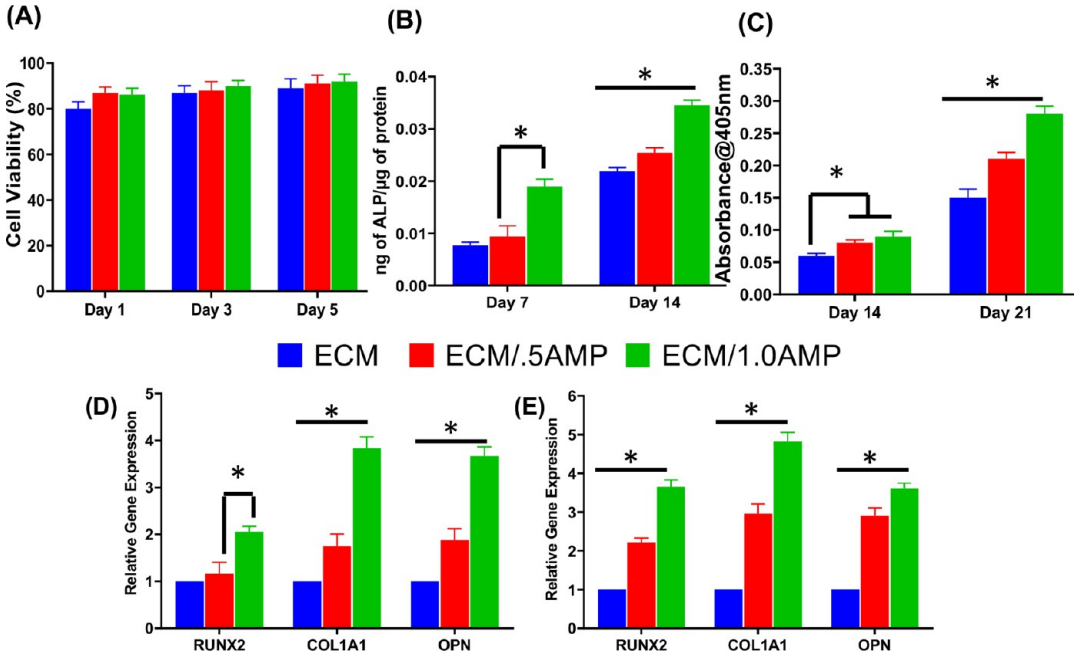

Figure 5. (A) Cell viability of DPSCs within the bioprinted constructs using ECM and AMP-modified bioinks is consistently above 90% for at least 5 days. (B−E) Osteogenic differentiation shows enhanced DPSCs' differentiation into functional osteoblasts capable of secreting a mineralized matrix. (B) ALP assay, (C) ARS assay, and (D,E) osteogenic gene expression at day 14 and 21 (*$p < 0.05$).

to assess the processing efficiency and overall cytocompatibility of the developed composite bioink. Representative fluorescence images of cell-laden bioink with and without AMP incorporation after 1, 3, and 5 days in culture are shown in Figure 4. Calcein staining showed homogenous cell distribution with high viability for all groups. Interestingly, DPSCs displayed an elongated morphology after 1 day within the ECM/AMP-bioprinted constructs, thus suggesting improved cell attachment. Of note, hydrogel properties, such as stiffness, density, and composition, can influence the cell morphology and function.[42,43] Herein, although the reasons could not be precisely identified, they might be due to the presence of AMP particles that can provide additional sites for cell attachment. Quantification of live and dead cells showed viable cells ∼90% up to 5 d in culture for all groups (Figure 5A). There was no statistically significant difference among the groups. Comparable trends have been observed when chitosan-hydroxyapatite and collagen-α-TCP hydrogels laden with MC3T3-E1 were printed.[33,44]

***In Vitro* Osteogenic Mineralization and Differentiation of DPSCs-Laden 3D Printed Constructs.** AMP is a biocompatible material containing several kinds of ions, which can diffuse to influence the cell behavior.[30,31] This positive effect can be attributed to the presence of Mg^{2+} ions that are well-known for their favorable effect on cellular activities.[45,46] Furthermore, these ions, released during the dissolution of incorporated AMP, were observed to influence the osteogenic differentiation of DPSCs in the present investigation. However, the potential application of AMP into hydrogels to create a bioink for bone tissue regeneration has not been previously studied. Hence, the AMP/ECM bioink formulation was investigated for its mineralization potential without the addition of osteogenic factors in the medium by alkaline phosphatase (ALP) and alizarin red staining (ARS) assays (Figure 5B,C). ALP activity was significantly increased on day 14 in both ECM/0.5AMP- and ECM/1.0AMP-bioprinted constructs, compared to their virgin (AMP-free) ECM counterparts. However, no significant difference in ALP expression at day 7 was observed between the AMP-free and ECM/0.5AMP-modified construct. ARS data showed enhanced DPSCs' capacity to secrete the mineralized matrix. After 14 and 21 days, ECM/0.5AMP and ECM/1.0AMP presented higher levels of mineralization compared to virgin ECM constructs, showing AMP particles' ability to drive osteogenic differentiation (Figure 5D,E). Additionally, DPSCs from extracted third molars are promising sources of multipotent stromal cells in tissue engineering.[47] DPSCs have higher osteogenic potential than MSCs derived from the bone marrow and can differentiate into both osteoblast and odontoblast lineages. Moreover, DPSCs can generate vessel-integrated bone tissue structures, which are essential for a large volume of bone reconstruction. Similar results were previously observed when DPSCs had been exposed to MgP incorporated into 3D nanofibrous gelatin/MgP hybrid scaffolds.[48] The increased bioactivity associated with AMP-modified constructs can be due to Mg^{2+} release, which has been reported to induce the formation of amorphous CaP.[29,31]

Osteogenic differentiation within the AMP-modified printed constructs was further studied *in vitro*. The mRNA expression of several osteogenic genes, including Runt-related transcription factor 2 (RUNX2), osteopontin (OPN), and collagen alpha 1 (COL1A1), was upregulated. At day 14, both ECM/0.5AMP and ECM/1.0AMP increased the expression of all osteogenic-related genes (except for RUNX2) compared to the ECM (Figure 5D). Compared to virgin ECM constructs, RUNX2 expression at day 21 was 2- and 3.6-fold higher in ECM/0.5AMP and ECM/1.0AMP constructs, respectively (Figure 5E). There was no significant difference between ECM/0.5AMP constructs compared to the ECM at day 14. ECM/1.0AMP constructs upregulated COL1A1 expression by 3.9 ± 0.23- and 4.8 ± 0.26-fold at day 21 compared to the virgin ECM construct. The 4-fold increase in OPN expression

https://dx.doi.org/10.1021/acsami.0c05311
ACS Appl. Mater. Interfaces 2020, 12, 23752−23763

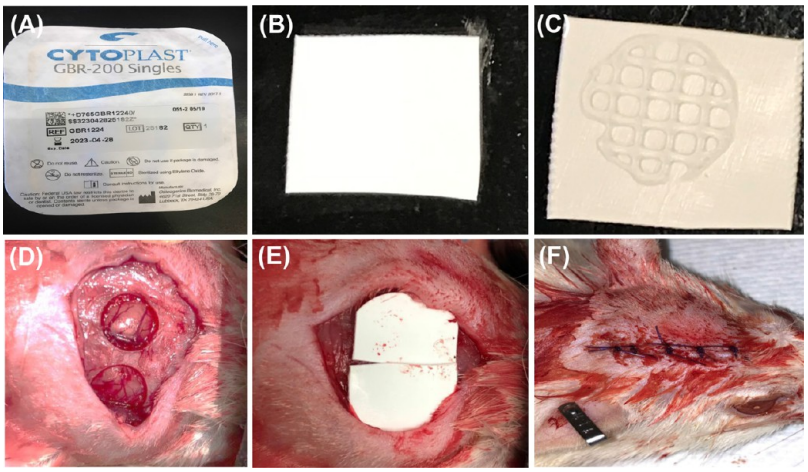

Figure 6. Steps of a critical sized bilateral defect procedure performed in rats. (A) PTFE membrane (Cytoplast) was used as a carrier for the printed construct, (B) PTFE membrane was cut in square-shaped pieces of *ca.* 7 × 7 mm^2, (C) bioprinted construct on the membrane, (D) prepared defect after irrigation, (E) implantation, and (F) suture.

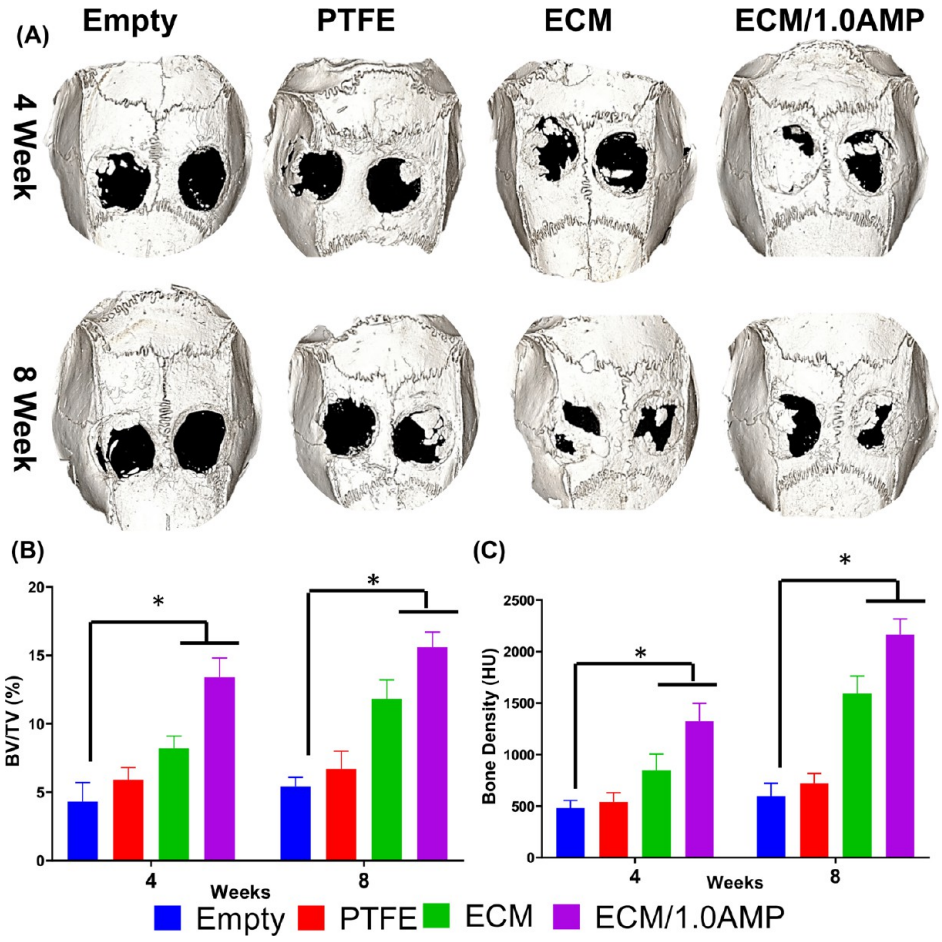

Figure 7. Micro-CT analysis. (A) Rat skull 3D rendering at 4- and 8-weeks. Calvarial defects that were left empty did not heal spontaneously for the duration of the study. In contrast, bone healing was gradually achieved when the defects were filled with either ECM or ECM/1.0AMP. (B,C) Bone parameters were quantified as % of tissue volume (BV/TV) within the defect and BD (HU). (*$p < 0.05$).

for ECM/1.0AMP constructs at days 14 and 21 strongly suggests osteoblastic differentiation and biomineralization. Our results are in line with the previously published data on MgP-based gels or Mg-doped hydrogels in terms of the upregulation of bone formation-related gene expression and mineralization.[48,49] Furthermore, it has been shown that AMP could stimulate the osteogenic differentiation of stem cells and osteoblasts.[29,30] However, in the present study, AMP-modified constructs favored *in vitro* mineralization without the use of a chemical inducer (*e.g.*, BMP2 or dexamethasone), thus underscoring the osteogenic potential of the formulated bioink. As there are no reports on the osteogenic differ-

https://dx.doi.org/10.1021/acsami.0c05311
ACS Appl. Mater. Interfaces 2020, 12, 23752−23763

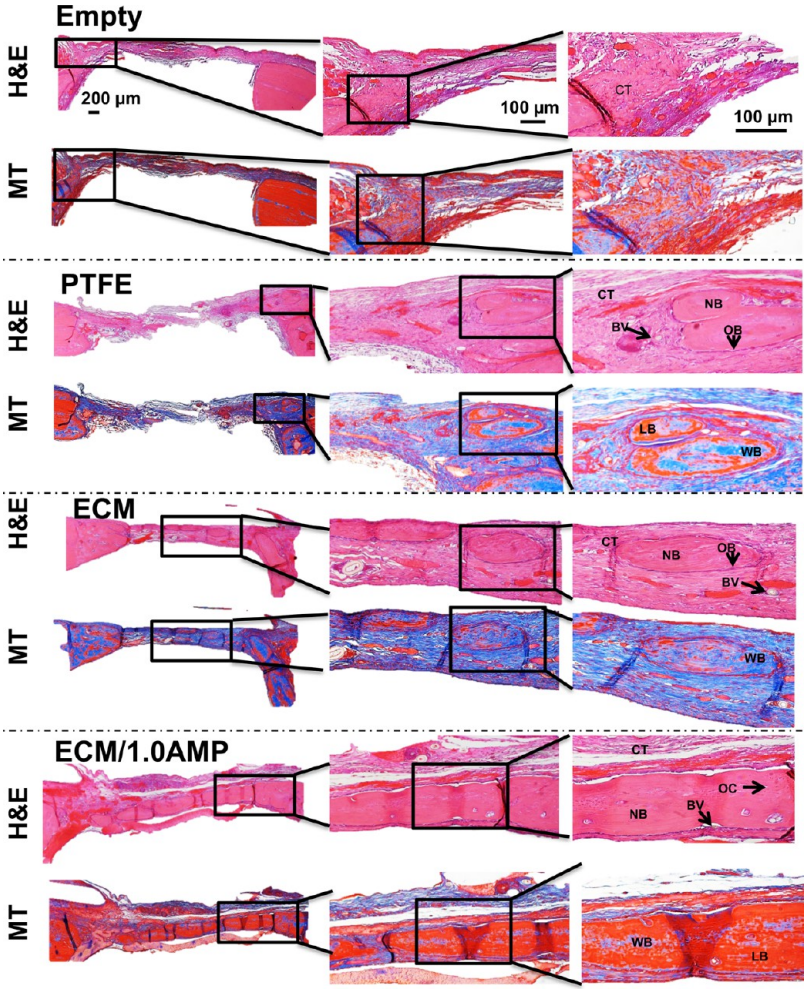

Figure 8. H&E and MT staining after 4 weeks, indicate healing of the defects with new bone formation restricted to an area close to the border of the defects. Connective tissue: CT, osteoblast: OB, new bone: NB, blood vessel: BV, osteocytes: OC, woven bone (blue): WB, lamellar bone (red): LB.

entiation of 3D-bioprinted DPSC-laden AMP-modified constructs, these insights are important steps toward the application of AMP in bioprinting for bone regeneration. Altogether, the data demonstrated that DPSC-laden AMP-modified hydrogels, in particular, the ECM/1.0AMP constructs, have significant osteogenic potential as exemplified by the *in vitro* onset of collagen synthesis, ECM maturation, and mineralization. This justified further *in vivo* testing of the developed ECM/AMP bioink.

***In Vivo* Bone Formation.** Considering that the clinical translation of cell-based strategies faces not only regulatory challenges but also risks of host immune reactions and uncontrolled cell differentiation,[50] we designed a critical-size rat calvarial defect model aiming to test our hypothesis that an AMP-modified ECM bioink would be valuable for bone regeneration and a suitable ink for *in situ* bioprinting. To that end, cell-free constructs were printed either with the virgin (AMP-free) ECM bioink or AMP-modified bioink (ECM/1.0AMP) on polytetrafluoroethylene (PTFE) membranes before implantation into rat cranial defects (Figure 6). The sham and PTFE membrane showed sparse bone formation; however, the ECM and ECM/1.0AMP displayed partial defect closure because of neo-formed bone islands. Qualitatively, Figure 7A shows the reconstruction of high-resolution images of bioink printed on the PTFE membrane obtained from micro-CT. Sham and PTFE-treated defects remained largely unfilled (opened) with minimal bone formation characterized by nonuniform low-density shadows at regions confined mostly to the defects' edges after 4 weeks.

In contrast, the ECM and ECM/1.0AMP displayed bone ingrowth from the defect margin toward the center of the defect, and the edges of the regenerated bone appear continuous with the surrounding bone. At 8 weeks, an increase in new bone formation in all groups compared to the sham was observed. However, bone regeneration was still incomplete at 8 weeks. In comparison with the ECM group, BV/TV for ECM/1.0AMP was ∼1.7- and 1.4-fold higher at 4 and 8 weeks, respectively (Figure 7B). Further, a significant increase in the bone density (BD) (Figure 7C) was observed in the ECM and ECM/1.0AMP from 4 to 8 weeks. These results demonstrated that the presence of AMP in the bioink significantly increased bone formation compared to sham, PTFE, and the virgin (*i.e.*, AMP-free) ECM group. This enhanced mineralization of the healing defects in the ECM/1.0AMP group is likely due to the stimulating effects of released Mg^{2+} ions, which are known to activate the differentiation of osteoblasts and mobilize minerals (calcium and phosphorus) from bone to the newly-formed ECM.[29,49,51]

Haematoxylin & eosin (H&E) staining showed the presence of loose collagen fibers, indicating that there was a minimal

https://dx.doi.org/10.1021/acsami.0c05311
ACS Appl. Mater. Interfaces 2020, 12, 23752−23763

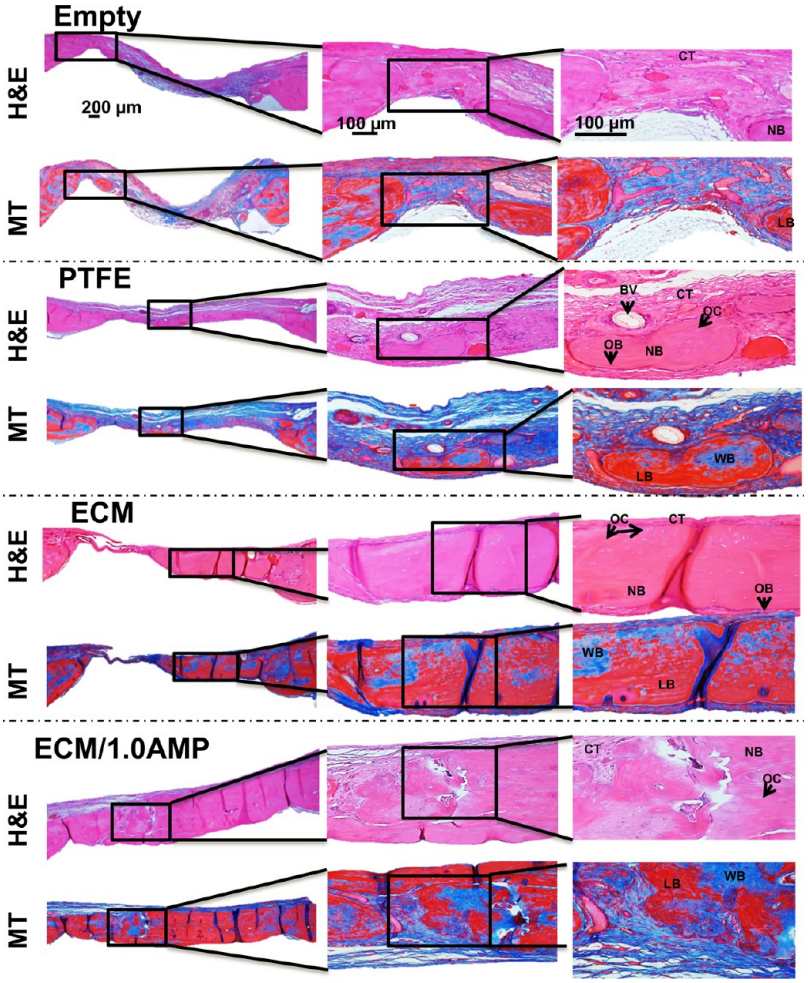

Figure 9. H&E and MT staining after 8 weeks indicate healing of the defects with new bone formation restricted to the area close to the border of the defects, with the ECM and ECM/1.0AMP showing thicker bone formation compared to 4 weeks. Connective tissue: CT, osteoblast: OB, new bone: NB, blood vessel: BV, osteocytes: OC, woven bone (blue): WB, lamellar bone (red): LB.

bone formation in the defect areas of the controls (Figures 8 and 9). In the ECM group, staining confirmed defect bridging from the host bone with tightly packed, large collagen fibers with less fibroblasts compared to regular connective tissue, indicating a significant amount of regenerated tissue. Importantly, the regenerated tissue showed osteocytes trapped in the lacunae and osteons, including the Haversian canals. The newly formed lamellar bone had a more similar morphology and density than that of the host bone. The defect area in the ECM/1.0AMP group was covered with dense regenerated bone tissue with a fibrous layer structure that was much more extensive than the ECM or control group.

A thin layer of blue stain, indicative of collagen fibers, was observed in Masson's trichrome (MT)-stained samples (Figures 8 and 9), which would not have mineralized in the case of empty defects and defects covered with the PTFE membrane. A previous study that evaluated bone formation of a peptide hydrogel injected inside a polyether ether ketone (PEEK) cage, implanted in the femoral condyle of rats, reported bridging the defect with a higher amount of calcium in hydrogel compared with the PEEK cage control.[52] A similar trend was observed in this study, where the ECM, itself, showed great osteoconductivity, which, in turn, led to significant bone formation. Conversely, the addition of AMP resulted in a greater presence of the woven and lamellar bone, resulting from osteoblastic osteoid formation causing defect restoration. The ECM and ECM/1.0AMP-treated defects showed an increase in thickness of the newly formed bone after 8 weeks, compared to 4 weeks. Thus, we concluded that the formulated ECM/1.0AMP composition performed an osteo-stimulating function *in vivo* not only by promoting new bone formation but also through a high degree of bone maturation. This finding is in agreement with previous studies that demonstrated the ability of MgP to induce regeneration of the new trabecular bone with osteoid-producing cells.[23,49,51] Interestingly, we did not observe any remaining AMP particles after 4 weeks of implantation, indicating a faster degradation of AMP. Likely, this allowed for the more rapid migration of osteogenic cells into the defect, resulting in enhanced neobone formation.

Growth factor-free bioinks are of great interest, as they allow a more realistic clinical translation due to their cost-effectiveness, while avoiding side-effects, such as edema, inflammation, and uncontrolled bone formation, commonly seen with the use of BMP2.[53] Despite our promising results, additional studies, including but not limited to chemical analysis (*e.g.*, Raman spectroscopy), should be carried out to provide a deeper understanding of the overall quality of the regenerated bone formed in the defect by the cell-free ECM/AMP-bioprinted construct when compared to the original

https://dx.doi.org/10.1021/acsami.0c05311
ACS Appl. Mater. Interfaces 2020, 12, 23752−23763

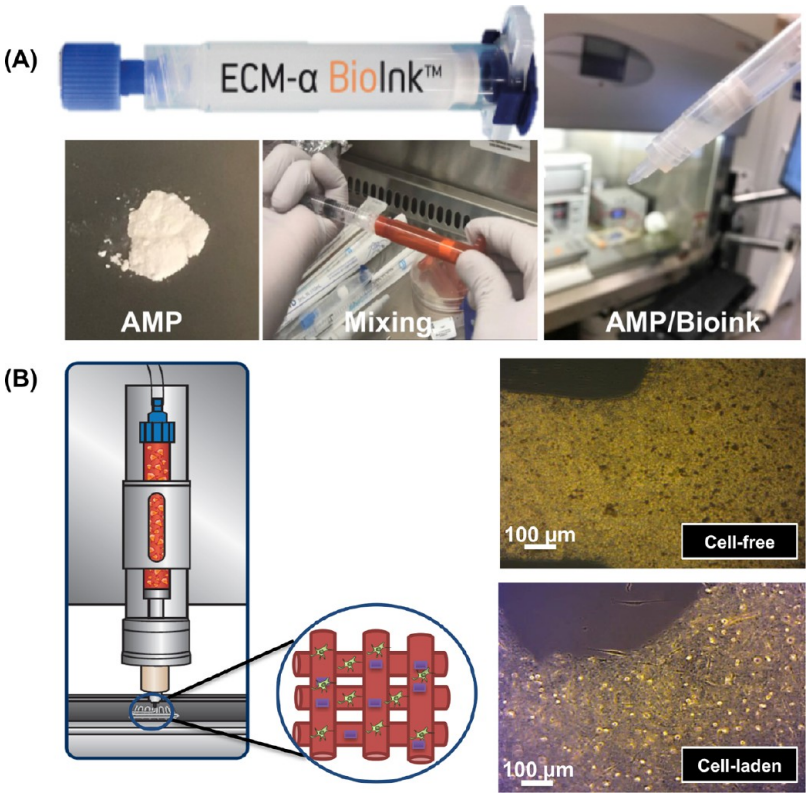

Figure 10. (A) Representative macrophotographs of the ECM/AMP bioink formulation process. (B) ECM/AMP cell-laden bioink printing and the optical images of the AMP-based cell-laden composites with and without cells.

bone. Nevertheless, the ECM/1.0AMP composition enabled the fabrication of constructs with reproducible microarchitectures, which also hold particular promise for *in situ* bioprinting strategies for bone regeneration. Thus, this novel AMP-based bioink has great potential for translation for the clinical use for bone tissue engineering applications.

CONCLUSIONS

Bioprinting is a useful fabrication tool that generates cell-laden 3D constructs that further replicate intricate compositional and architectural organization of tissues. Nevertheless, the formulation of bioink with desirable rheological properties and improved cell viability is a prerequisite for the development of functional tissue constructs for the restoration of large craniomaxillofacial bone defects. Here, we engineered ECM/AMP composite bioink compositions for bone regeneration. The formulated bioink showed printability similar to the virgin ECM hydrogel. Furthermore, DPSCs showed an elongated morphology in ECM/AMP-bioprinted constructs. Importantly, compared to the ECM bioink, the ECM/AMP formulations showed improved osteogenic differentiation without the need for chemical inducers, suggesting that the AMP presence was able to trigger osteogenic differentiation of the encapsulated DPSCs. Moreover, the ECM/1.0AMP composition displayed excellent bone regeneration capability *in vivo*, underscoring its potential as a novel bioink also for *in situ* printing. Therefore, in future studies, we will focus on improving the print resolution to match the defect-specific anatomy to make it possible to accelerate new bone formation by printing directly into the defect using the developed ECM/AMP bioink.

MATERIALS AND METHODS

Materials and Reagents. As a cell carrier material, the ECM-α hydrogel (2% octapeptide FEFEFKFK and 98% water) was procured from regenHU (regenHU, Villaz-St-Pierre, Switzerland). Magnesium nitrate hexahydrate and diammonium hydrogen phosphates were procured from Sigma-Aldrich (St. Louis, MO, USA). Alpha-modified Eagle's medium (α-MEM), fetal bovine serum (FBS), penicillin−streptomycin, Dulbecco's phosphate-buffered saline (PBS), and trypsin were obtained from Gibco-Invitrogen (San Diego, CA, USA). Stains, such as calcein-AM (Thermo Fisher Scientific, Inc., Waltham, MA, USA) and propidium iodide (PI) (Sigma-Aldrich), were used as needed.

Synthesis of the Cell-Laden ECM/AMP Composite Bioink. A commercially available ECM-based hydrogel (ECM-α) containing 2% octapeptide FEFEFKFK and 98% water was used. This octapeptide FEFEFKFK-based hydrogel is an ionic-complementary peptide that self-assembles where F is noncharged and hydrophobic, and E and K are negatively and positively charged, respectively, at physiological pH. FEFEFKFK self-assembles into an antiparallel β-sheet secondary structure, where all F's are placed on the same side of the β-sheet, while the charged amino acids are located on the other side. This peptide subsequently forms a network of β-sheet-rich nanofibers, which branch to form a 3D self-supporting hydrogel, depending on the pH, temperature, controllable mechanical properties, and ionic strength of the media. AMP particles were synthesized using a microwave-assisted route at a fixed molar ratio (Mg/P = 2:1), as described in our previous work.[30] AMP/ECM bioink was formulated by dispersing previously sieved AMP micron-sized particles (∼45 μm) into the ECM hydrogel. Briefly, 0.5 and 1% AMP (% w/w) were mixed with the ECM hydrogel using a female−female luer connector.

Chemical, Morphological, and Mechanical Characterization of Bioink. Attenuated total reflectance/FTIR spectroscopy (Thermo Nicolet IS-50, Thermo Fisher Scientific Inc., Waltham MA, USA) was carried out to study the interaction of the incorporated AMP into the ECM hydrogel. Data were recorded at room temperature and in the spectral range of 4000−520 cm^{-1}, utilizing a 16 scan per sample.

https://dx.doi.org/10.1021/acsami.0c05311
ACS Appl. Mater. Interfaces 2020, 12, 23752−23763

Baseline correction spectra were then centered and normalized for analysis. The morphology, AMP distribution, and chemical composition of the formulated bioinks were investigated by field emission SEM (Tescan MIRA3 FEG-SEM, Tescan USA Inc., Warrendale, PA, USA) and EDS. The formulated bioinks were injected directly onto double sided carbon tape mounted on a SEM prior to imaging at various magnifications.

Rheological properties of the formulated bioink were investigated using a rheometer (Discovery HR-2, TA Instruments, New Castle, DE, USA) equipped with a pair of 20 mm parallel plates. In each experiment, 200 μL of the formulated inks were loaded onto the stage and the upper plate was lowered until a 300 μm gap was reached. All readings were taken at 37 °C. Amplitude sweeps were performed at least once for each sample at a fixed frequency of 1 Hz in the 0.1−10% strain range to determine the linear viscoelastic region (LVR). Frequency sweeps were then performed at 1% strain, within the LVR of the samples. Thereafter, storage modulus (G') and loss modulus (G'') were recorded at a 0.2% strain and frequency of 1 Hz. All measurements were repeated at least three times to ensure reproducibility.

Bioink Printability. All the formulated bioinks were printed using a cell-friendly print head (regenHU, Villaz-St-Pierre, Switzerland) controlled by an electromagnetic microvalve system and compressed air in a Class II biosafety cabinet permitting work under sterile conditions (3DDiscovery, regenHU). Printing path designs were created using BioCAD software (regenHU); a G-code file was obtained, loaded to HMI software, and launched for printing. To prevent sedimentation in the printing, a cell mixing system (regenHU) was used to print the designed constructs with a homogeneous distribution of cells and AMP particles. An optical microscope (Zeiss Stemi 508, Carl Zeiss Meditec AG, Oberkochen, Germany) in bright field mode was used to determine the state of distribution of the AMP particles in printed constructs. The print accuracy was evaluated qualitatively using a digital scanner (V550, Epson America, Inc., Long Beach, CA, USA) and the optimized feed rate and dosing distance were used for subsequent prints (Figure 10). Four-layer (10 mm × 10 mm) constructs were printed following optimized parameters (Table 1) to assess shape fidelity.

Table 1. Optimized Bioprinting Parameters of the ECM/AMP Bioink

printing parameters	ECM	ECM/0.5AMP	ECM/1.0AMP
extrusion pressure (MPa)	0.05	0.05	0.03
feed rate (mm/s)	15	16	20
dosing distance (mm)	0.1	0.1	0.16
valve opening time (μs)	110	110	110

***In Vitro* Cell Culture and Encapsulation.** Previously isolated and characterized DPSCs from human third molars were used.[54] In brief, the minced pulp tissue was digested in collagenase type I and dispase at 37 °C for 1 h, following single cell suspension obtained using a 70 μm strainer that was cultured and expanded. For the analysis, DPSCs from passages 3−6 were cultured in α-MEM supplemented with 10% (v/v) FBS and 1% (v/v) penicillin−streptomycin at 37 °C in a humidified atmosphere containing 5% CO_2. Upon confluency, the DPSCs were dissociated using trypsin, centrifuged, and 1×10^6 cells were carefully suspended in 50 μL of fresh medium and encapsulated in 950 μL of ECM or AMP/ECM bioinks and mixed homogeneously using a female−female luer connector under sterile conditions and used for all *in vitro* culture assays.

***In Vitro* Cell Viability of DPSC-Laden 3D-Bioprinted Constructs.** The viability of encapsulated DPSCs within bioprinted constructs was quantified up to 5 days postprinting using calcein-AM and PI. In brief, cell-laden printed constructs were washed (2×) with PBS and subsequently incubated at 37 °C in a staining solution for 30 min. Images were then taken using an inverted fluorescence microscope (Keyence BZ-X 710, Keyence Corporation of America, Itasca, IL, USA). The quantification of live and dead cells was done using MATLAB software for three samples per group and reported as a percentage of live/total cells.

***In Vitro* Osteogenic Differentiation of DPSC-Laden 3D-Bioprinted Constructs.** To determine the influence of AMP on the osteogenic potential of DPSCs, cell-laden ECM-based 3D-bioprinted constructs containing distinct (0.5 and 1%) AMP amounts were assessed using ALP activity and ARS assays. ALP activity was determined using the SensoLyte pNPP ALP Assay Kit Colorimeter (AnaSpec Inc., Fremont, CA, USA), following the manufacturer's instructions on days 7 and 14. Briefly, the cells were washed twice with PBS and harvested in assay buffer with 1% Triton-100. The collected cell suspension was incubated at 4 °C under agitation for 10 min. Aliquots of the extract were mixed with *para*-nitrophenyl phosphate (pNPP) substrate solution. The absorbance of aliquots was measured using a microplate reader (SpectraMax iD3, Molecular Devices LLC, San Jose, CA, USA) at a wavelength of 405 nm. The measured ALP deposition levels of the cell-laden structure were normalized by the measured ALP deposition levels of the cell-free structures and total protein content of each construct. All data values were defined as ±standard deviation (SD, $n = 4$). For the alizarin red assay, cells at days 14 and 21 were fixed in 4% formaldehyde at RT for 30 min and washed (2×) with PBS. The cells were stained with 40 mM ARS (pH 4.2) for 30 min at RT and destained using 10% acetic acid and ammonium hydroxide. The absorbance of aliquots was measured using a microplate reader at a wavelength of 405 nm.

***In Vitro* Evaluation of Osteogenic Markers by the Real-Time Polymerase Chain Reaction.** An real-time polymerase chain reaction (RT-PCR) evaluation was performed after 14 and 21 days of culture to measure the expression levels of the osteoblastic genes of the DPSCs, including RUNX2, COL1A1, and OPN. The TRIzol reagent (Invitrogen Life Technologies, Carlsbad, CA, USA) was used to isolate the total RNA from the cultured DPSCs. The concentration and purity of the isolated RNA were examined using a spectrophotometer (SpectraMax iD3). A complementary DNA (cDNA) synthesis from the RNase-free DNase-treated total RNA was performed with a reverse transcription system using the ReverTra Ace qPCR RT Master Mix (Applied Biosystems, Foster City, CA, USA). To conduct a quantitative RT-PCR, a StepOnePlus RT-PCR System (Applied Biosystems) was used to amplify the cDNA. The $\Delta\Delta C_q$ method was used to calculate the relative gene expression from quantification cycle values obtained by the quantitative RT-PCR.

***In Vivo* Bone Regeneration.** Sixteen 6-week old Fischer 344 male rats weighing *ca.* 300−320 g were procured from Envigo RMS, Inc. (Oxford, MI, USA) and used in this study. All the animal experiments were approved by the Ethics Committee on Animal Experimentation at the University of Michigan, and the surgeries were performed under the local Animal Care and Use Committee (IACUC, PRO00008502). All surgical procedures were performed under general anesthesia using 4% isoflurane (Piramal Critical Care Inc., Bethlehem, PA, USA) for induction, followed by maintenance with 2% isoflurane. The rat head was shaved, and the surgical site was cleaned with a povidone−iodine solution (Piramal Critical Care Inc.). A midline sagittal incision was made in the skull, and the scalp was elevated to expose the calvaria. Full-thickness critical-size bilateral defects (5 mm in diameter) were created using a trephine bur (Trephines 229XL RA; L Size #229XL-050-RAL, 5.0 mm inside/6.0 mm outside diameter, Meisinger USA, LLC, Centennial, CO, USA) attached to a dental handpiece with a micromotor operating at 800 rpm or less. Constant sterile saline was irrigated to avoid a heat-generated injury during surgery. The ECM and ECM/1.0AMP constructs were printed on the FDA-approved and commercially available nonresorbable PTFE membrane (Cytoplast GBR-200 Singles, Osteogenics Biomedical, Lubbock, TX, USA) and then transplanted into the defects (Figure 6). The rats were randomly allocated into four groups as follows: Sham (defect only), PTFE, ECM, and ECM/1.0AMP. The incision was closed with Vicryl 3−0 (Ethicon, Inc., Somerville, NJ, USA) resorbable sutures. After 4 and 8 weeks, the animals ($n = 4$/group) were euthanized by CO_2, and the calvaria of the rats was harvested, skin, and muscle tissue were

https://dx.doi.org/10.1021/acsami.0c05311
ACS Appl. Mater. Interfaces 2020, 12, 23752−23763

removed, followed by immersion of the bone/construct in a 4% paraformaldehyde solution for further tomographic and histological analysis.

Micro-computed Tomography. Nondestructive analysis of the newly formed bone at the bone defect was performed using μCT (Scanco μCT 100 Medical AG, Brüttisellen, Zurich, Switzerland). Samples were scanned at 70 kV and 114 μA and with a voxel size of 25 μm. The reconstructed 3D image was then traced to the circumference of the original defect, which, hereafter, was referred to as the region of interest (ROI). The bone volume fraction (BV/TV) and BD in Hounsfield units were calculated using ROI around the critical-size defect.

Histological Analysis. After the μCT scans, histological analyses consisting of H&E staining for cellularity and MT staining for bone formation were performed. Briefly, the specimens were decalcified in a 10% formic acid solution (Shandon TBD-1, Thermo Fisher Scientific Inc.), followed by dehydration in a series of ethanol solutions of increasing concentration until pure ethanol was reached. The specimens were embedded in paraffin and sectioned into 4 μm slices. The sections were stained and observed using a digital camera equipped with a light microscope (Nikon E800, Nikon Corporation, Tokyo, Japan).

Statistics. All values were expressed as mean ± SD of three independent experiments. Statistical analysis was performed using one-way analysis of variance, followed by Kruskal–Wallis posthoc tests (α = 0.05).

AUTHOR INFORMATION

Corresponding Author

Marco C. Bottino – *Department of Cariology, Restorative Sciences and Endodontics, School of Dentistry, University of Michigan, Ann Arbor, Michigan 48109-1078, United States;* orcid.org/0000-0001-8740-2464; Phone: +1-734.763.2206; Email: mbottino@umich.edu; Fax: +1-734.936.1597

Authors

Nileshkumar Dubey – *Department of Cariology, Restorative Sciences and Endodontics, School of Dentistry, University of Michigan, Ann Arbor, Michigan 48109-1078, United States*

Jessica A. Ferreira – *Department of Cariology, Restorative Sciences and Endodontics, School of Dentistry, University of Michigan, Ann Arbor, Michigan 48109-1078, United States;* orcid.org/0000-0002-9669-4339

Jos Malda – *Regenerative Medicine Center and Department of Orthopedics, University Medical Center Utrecht, Utrecht 3584 CX, The Netherlands; Department of Clinical Sciences, Faculty of Veterinary Medicine, Utrecht University, Utrecht 3584 CL, The Netherlands;* orcid.org/0000-0002-9241-7676

Sarit B. Bhaduri – *Department of Mechanical, Industrial and Manufacturing Engineering and Surgery (Dentistry), University of Toledo, Toledo, Ohio 43606, United States; EEC Division, Directorate of Engineering, The National Science Foundation, Alexandria, Virginia 22314, United States*

Complete contact information is available at: https://pubs.acs.org/10.1021/acsami.0c05311

Notes

The authors declare no competing financial interest.

ACKNOWLEDGMENTS

The authors thank Osteogenics Biomedical for donating the PTFE membranes (Cytoplast GBR-200). M.C.B. acknowledges the National Institutes of Health (NIH)/National Institute of Dental and Craniofacial Research (NIDCR) (Grants K08DE023552 and R01DE026578). The content is solely the responsibility of the authors and does not necessarily represent the official views of the National Institutes of Health.

REFERENCES

(1) Bodic, F.; Hamel, L.; Lerouxel, E.; Baslé, M. F.; Chappard, D. Bone loss and teeth. *Jt., Bone, Spine* **2005**, *72*, 215–221.

(2) Loi, F.; Córdova, L. A.; Pajarinen, J.; Lin, T.-h.; Yao, Z.; Goodman, S. B. Inflammation, fracture and bone repair. *Bone* **2016**, *86*, 119–130.

(3) Chen, Y.; Xu, J.; Huang, Z.; Yu, M.; Zhang, Y.; Chen, H.; Ma, Z.; Liao, H.; Hu, J. An innovative approach for enhancing bone defect healing using plga scaffolds seeded with extracorporeal-shock-wave-treated bone marrow mesenchymal stem cells (BMSCS). *Sci. Rep.* **2017**, *7*, 44130.

(4) Qu, H.; Fu, H.; Han, Z.; Sun, Y. Biomaterials for bone tissue engineering scaffolds: a review. *RSC Adv.* **2019**, *9*, 26252–26262.

(5) Bottino, M. C.; Thomas, V.; Schmidt, G.; Vohra, Y. K.; Chu, T.-M. G.; Kowolik, M. J.; Janowski, G. M. Recent advances in the development of GTR/GBR membranes for periodontal regeneration-A materials perspective. *Dent. Mater.* **2012**, *28*, 703–721.

(6) Wüst, S.; Müller, R.; Hofmann, S. Controlled Positioning of Cells in Biomaterials-Approaches Towards 3D Tissue Printing. *J. Funct. Biomater.* **2011**, *2*, 119–154.

(7) Boland, T.; Tao, X.; Damon, B. J.; Manley, B.; Kesari, P.; Jalota, S.; Bhaduri, S. Drop-on-demand printing of cells and materials for designer tissue constructs. *Mater. Sci. Eng., C* **2007**, *27*, 372–376.

(8) Hölzl, K.; Lin, S.; Tytgat, L.; Van Vlierberghe, S.; Gu, L.; Ovsianikov, A. Bioink properties before, during and after 3D bioprinting. *Biofabrication* **2016**, *8*, 032002.

(9) Gudapati, H.; Dey, M.; Ozbolat, I. A comprehensive review on droplet-based bioprinting: past, present and future. *Biomaterials* **2016**, *102*, 20–42.

(10) Ng, W. L.; Lee, J. M.; Yeong, W. Y.; Win Naing, M. Microvalve-based bioprinting - process, bio-inks and applications. *Biomater. Sci.* **2017**, *5*, 632–647.

(11) Athirasala, A.; Tahayeri, A.; Thrivikraman, G.; França, C. M.; Monteiro, N.; Tran, V.; Ferracane, J.; Bertassoni, L. E. A dentin-derived hydrogel bioink for 3D bioprinting of cell laden scaffolds for regenerative dentistry. *Biofabrication* **2018**, *10*, 024101.

(12) Levato, R.; Jungst, T.; Scheuring, R.; Blunk, T.; Groll, J.; Malda, J. From Shape to Function: The Next Step in Bioprinting. *Adv. Mater.* **2020**, *32*, 1906423.

(13) Laternser, S.; Keller, H.; Leupin, O.; Rausch, M.; Graf-Hausner, U.; Rimann, M. A Novel Microplate 3D Bioprinting Platform for the Engineering of Muscle and Tendon Tissues. *SLAS Technol.* **2018**, *23*, 599–613.

(14) Ferris, C. J.; Gilmore, K. J.; Beirne, S.; McCallum, D.; Wallace, G. G.; in het Panhuis, M. Bio-ink for on-demand printing of living cells. *Biomater. Sci.* **2013**, *1*, 224–230.

(15) Blaeser, A.; Duarte Campos, D. F.; Puster, U.; Richtering, W.; Stevens, M. M.; Fischer, H. Controlling shear stress in 3D bioprinting is a key factor to balance printing resolution and stem cell integrity. *Adv. Healthcare Mater.* **2016**, *5*, 326–333.

(16) He, Y.; Yang, F.; Zhao, H.; Gao, Q.; Xia, B.; Fu, J. Research on the printability of hydrogels in 3D bioprinting. *Sci. Rep.* **2016**, *6*, 29977.

(17) Ashammakhi, N.; Ahadian, S.; Pountos, I.; Hu, S.-K.; Tellisi, N.; Bandaru, P.; Ostrovidov, S.; Dokmeci, M. R.; Khademhosseini, A. In situ three-dimensional printing for reparative and regenerative therapy. *Biomed. Microdevices* **2019**, *21*, 42.

(18) Tibbitt, M. W.; Anseth, K. S. Hydrogels as extracellular matrix mimics for 3D cell culture. *Biotechnol. Bioeng.* **2009**, *103*, 655–663.

(19) Shim, J.-H.; Jang, K.-M.; Hahn, S. K.; Park, J. Y.; Jung, H.; Oh, K.; Park, K. M.; Yeom, J.; Park, S. H.; Kim, S. W.; Wang, J. H.; Kim, K.; Cho, D.-W. Three-dimensional bioprinting of multilayered constructs containing human mesenchymal stromal cells for

osteochondral tissue regeneration in the rabbit knee joint. *Biofabrication* **2016**, *8*, 014102.
(20) Hong, Y.; Legge, R. L.; Zhang, S.; Chen, P. Effect of amino acid sequence and pH on nanofiber formation of self-assembling peptides EAK16-II and EAK16-IV. *Biomacromolecules* **2003**, *4*, 1433−1442.
(21) Saiani, A.; Mohammed, A.; Frielinghaus, H.; Collins, R.; Hodson, N.; Kielty, C. M.; Sherratt, M. J.; Miller, A. F. Self-assembly and gelation properties of α-helix versus β-sheet forming peptides. *Soft Matter* **2009**, *5*, 193−202.
(22) Huang, W.-S.; Chu, I.-M. Injectable polypeptide hydrogel/inorganic nanoparticle composites for bone tissue engineering. *PLoS One* **2019**, *14*, No. e0210285.
(23) Klammert, U.; Ignatius, A.; Wolfram, U.; Reuther, T.; Gbureck, U. In vivo degradation of low temperature calcium and magnesium phosphate ceramics in a heterotopic model. *Acta Biomater.* **2011**, *7*, 3469−3475.
(24) Kanter, B.; Geffers, M.; Ignatius, A.; Gbureck, U. Control of in vivo mineral bone cement degradation. *Acta Biomater.* **2014**, *10*, 3279−3287.
(25) Klammert, U.; Vorndran, E.; Reuther, T.; Müller, F. A.; Zorn, K.; Gbureck, U. Low temperature fabrication of magnesium phosphate cement scaffolds by 3D powder printing. *J. Mater. Sci.: Mater. Med.* **2010**, *21*, 2947−2953.
(26) Nabiyouni, M.; Brückner, T.; Zhou, H.; Gbureck, U.; Bhaduri, S. B. Magnesium-based bioceramics in orthopedic applications. *Acta Biomater.* **2018**, *66*, 23−43.
(27) Ostrowski, N.; Roy, A.; Kumta, P. N. Magnesium phosphate cement systems for hard tissue applications: a review. *ACS Biomater. Sci. Eng.* **2016**, *2*, 1067−1083.
(28) Chen, Y.; Wang, Y.; Yang, Q.; Liao, Y.; Zhu, B.; Zhao, G.; Shen, R.; Lu, X.; Qu, S. A novel thixotropic magnesium phosphate-based bioink with excellent printability for application in 3D printing. *J. Mater. Chem. B* **2018**, *6*, 4502−4513.
(29) Ostrowski, N.; Lee, B.; Hong, D.; Enick, P. N.; Roy, A.; Kumta, P. N. Synthesis, osteoblast, and osteoclast viability of amorphous and crystalline tri-magnesium phosphate. *ACS Biomater. Sci. Eng.* **2014**, *1*, 52−63.
(30) Babaie, E.; Lin, B.; Goel, V. K.; Bhaduri, S. B. Evaluation of amorphous magnesium phosphate (AMP) based non-exothermic orthopedic cements. *Biomed. Mater.* **2016**, *11*, 055010.
(31) Zhou, H.; Nabiyouni, M.; Lin, B.; Bhaduri, S. B. Fabrication of novel poly(lactic acid)/amorphous magnesium phosphate bionanocomposite fibers for tissue engineering applications via electrospinning. *Mater. Sci. Eng., C* **2013**, *33*, 2302−2310.
(32) Kim, W.; Kim, G. Collagen/bioceramic-based composite bioink to fabricate a porous 3D hASCs-laden structure for bone tissue regeneration. *Biofabrication* **2019**, *12*, 015007.
(33) Kim, W. J.; Yun, H.-S.; Kim, G. H. An innovative cell-laden α-TCP/collagen scaffold fabricated using a two-step printing process for potential application in regenerating hard tissues. *Sci. Rep.* **2017**, *7*, 3181.
(34) Kwon, H.-K.; Park, D.-G. Infra-red study of surface carbonation on polycrystalline magnesium hydroxide. *Bull. Korean Chem. Soc.* **2009**, *30*, 2567−2573.
(35) Ahlfeld, T.; Doberenz, F.; Kilian, D.; Vater, C.; Korn, P.; Lauer, G.; Lode, A.; Gelinsky, M. Bioprinting of mineralized constructs utilizing multichannel plotting of a self-setting calcium phosphate cement and a cell-laden bioink. *Biofabrication* **2018**, *10*, 045002.
(36) Loo, Y.; Hauser, C. A. E. Bioprinting synthetic self-assembling peptide hydrogels for biomedical applications. *Biomed. Mater.* **2015**, *11*, 014103.
(37) Castillo Diaz, L. A.; Elsawy, M.; Saiani, A.; Gough, J. E.; Miller, A. F. Osteogenic differentiation of human mesenchymal stem cells promotes mineralization within a biodegradable peptide hydrogel. *J. Tissue Eng.* **2016**, *7*, 2041731416649789.
(38) Panwar, A.; Tan, L. Current status of bioinks for micro-extrusion-based 3D bioprinting. *Molecules* **2016**, *21*, 685.
(39) Mueller, S.; Llewellin, E. W.; Mader, H. M. The rheology of suspensions of solid particles. *Proc. R. Soc. A* **2009**, *466*, 1201−1228.
(40) Xu, C.; Zhang, M.; Huang, Y.; Ogale, A.; Fu, J.; Markwald, R. R. Study of droplet formation process during drop-on-demand inkjetting of living cell-laden bioink. *Langmuir* **2014**, *30*, 9130−9138.
(41) Cidonio, G.; Glinka, M.; Dawson, J.; Oreffo, R. O. C. The cell in the ink: Improving biofabrication by printing stem cells for skeletal regenerative medicine. *Biomaterials* **2019**, *209*, 10−24.
(42) Tusan, C. G.; Man, Y.-H.; Zarkoob, H.; Johnston, D. A.; Andriotis, O. G.; Thurner, P. J.; Yang, S.; Sander, E. A.; Gentleman, E.; Sengers, B. G.; Evans, N. D. Collective cell behavior in mechanosensing of substrate thickness. *Biophys. J.* **2018**, *114*, 2743−2755.
(43) Ahearne, M. Introduction to cell-hydrogel mechanosensing. *Interface Focus* **2014**, *4*, 20130038.
(44) Demirtaş, T. T.; Irmak, G.; Gümüşderelioğlu, M. A bioprintable form of chitosan hydrogel for bone tissue engineering. *Biofabrication* **2017**, *9*, 035003.
(45) Sikder, P.; Grice, C. R.; Lin, B.; Goel, V. K.; Bhaduri, S. B. Single-phase, antibacterial trimagnesium phosphate hydrate coatings on polyetheretherketone (PEEK) implants by rapid microwave irradiation technique. *ACS Biomater. Sci. Eng.* **2018**, *4*, 2767−2783.
(46) Sikder, P.; Grice, C.; Bhaduri, S. B. Processing-structure-property correlations of crystalline antibacterial magnesium phosphate (newberyite) coatings and their in vitro effect. *Surf. Coat. Technol.* **2019**, *374*, 276−290.
(47) d'Aquino, R.; Graziano, A.; Sampaolesi, M.; Laino, G.; Pirozzi, G.; De Rosa, A.; Papaccio, G. Human postnatal dental pulp cells co-differentiate into osteoblasts and endotheliocytes: a pivotal synergy leading to adult bone tissue formation. *Cell Death Differ.* **2007**, *14*, 1162.
(48) Qu, T.; Jing, J.; Jiang, Y.; Taylor, R. J.; Feng, J. Q.; Geiger, B.; Liu, X. Magnesium-containing nanostructured hybrid scaffolds for enhanced dentin regeneration. *Tissue Eng., Part A* **2014**, *20*, 2422−2433.
(49) Laurenti, M.; Al Subaie, A.; Abdallah, M.-N.; Cortes, A. R. G.; Ackerman, J. L.; Vali, H.; Basu, K.; Zhang, Y. L.; Murshed, M.; Strandman, S.; Zhu, J.; Makhoul, N.; Barralet, J. E.; Tamimi, F. Two-dimensional magnesium phosphate nanosheets form highly thixotropic gels that up-regulate bone formation. *Nano Lett.* **2016**, *16*, 4779−4787.
(50) Wang, S. J.; Jiang, D.; Zhang, Z. Z.; Chen, Y. R.; Yang, Z. D.; Zhang, J. Y.; Shi, J.; Wang, X.; Yu, J. K. Biomimetic Nanosilica-Collagen Scaffolds for In Situ Bone Regeneration: Toward a Cell-Free, One-Step Surgery. *Adv. Mater.* **2019**, *31*, 1904341.
(51) Kim, J.-A.; Lim, J.; Naren, R.; Yun, H.-s.; Park, E. K. Effect of the biodegradation rate controlled by pore structures in magnesium phosphate ceramic scaffolds on bone tissue regeneration in vivo. *Acta Biomater.* **2016**, *44*, 155−167.
(52) Ando, K.; Imagama, S.; Kobayashi, K.; Ito, K.; Tsushima, M.; Morozumi, M.; Tanaka, S.; Machino, M.; Ota, K.; Nishida, K.; Nishida, Y.; Ishiguro, N. Effects of a self-assembling peptide as a scaffold on bone formation in a defect. *PLoS One* **2018**, *13*, No. e0190833.
(53) Fujioka-Kobayashi, M.; Ota, M. S.; Shimoda, A.; Nakahama, K.-i.; Akiyoshi, K.; Miyamoto, Y.; Iseki, S. Cholesteryl group- and acryloyl group-bearing pullulan nanogel to deliver BMP2 and FGF18 for bone tissue engineering. *Biomaterials* **2012**, *33*, 7613−7620.
(54) Silva, G. O.; Zhang, Z.; Cucco, C.; Oh, M.; Camargo, C. H. R.; Nör, J. E. Lipoprotein Receptor-related Protein 6 Signaling is Necessary for Vasculogenic Differentiation of Human Dental Pulp Stem Cells. *J. Endod.* **2017**, *43*, S25−S30.

https://dx.doi.org/10.1021/acsami.0c05311
ACS Appl. Mater. Interfaces 2020, 12, 23752−23763